Check for updates

Porous Materials Hot Paper

How to cite:
International Edition: doi.org/10.1002/anie.202102337
German Edition: doi.org/10.1002/ange.202102337

Porous Covalent Organic Polymers for Efficient Fluorocarbon-Based Adsorption Cooling

Jian Zheng[+], Mohammad Wahiduzzaman[+], Dushyant Barpaga[+], Benjamin A. Trump, Oliver Y. Gutiérrez, Praveen Thallapally, Shengqian Ma, B. Peter McGrail, Guillaume Maurin, and Radha Kishan Motkuri**

Abstract: *Adsorption-based cooling is an energy-efficient renewable-energy technology that can be driven using low-grade industrial waste heat and/or solar heat. Here, we report the first exploration of fluorocarbon adsorption using porous covalent organic polymers (COPs) for this cooling application. High fluorocarbon R134a equilibrium capacities and unique overall linear-shaped isotherms are revealed for the materials, namely COP-2 and COP-3. The key role of mesoporous defects on this unusual adsorption behavior was demonstrated by molecular simulations based on atomistic defect-containing models built for both porous COPs. Analysis of simulated R134a adsorption isotherms for various defect-containing atomistic models of the COPs shows a direct correlation between higher fluorocarbon adsorption capacities and increasing pore volumes induced by defects. Combined with their high porosities, excellent reversibility, fast kinetics, and large operating window, these defect-containing porous COPs are promising for adsorption-based cooling applications.*

Introduction

Porous organic frameworks (POFs) are a class of nanoporous materials constructed using reticular chemistry with organic building monomers linked by strong covalent bonds.[1] POF structures, including covalent organic polymers (COPs), covalent organic frameworks (COFs), covalent triazine frameworks (CTFs), and porous aromatic frameworks (PAFs) among others, contain only light elements since they are assembled using linkers such as boronates, imines, borosilicates, triazines, and hydrazones.[2] The building blocks form rigid structures that can be tuned based on the choice of monomers and appropriate polymerization reactions.[1c] Such controllable pore structures, with high porosity and low density offer a great opportunity to achieve high gravimetric guest uptake for storage applications.[3] More importantly, in contrast to metal-organic frameworks (MOFs), the absence of metal elements in the confined pore wall of COPs ensures moderate host-guest interactions to improve the reversibility and kinetics of gas adsorption-desorption cycles which is of utmost importance for gas storage and release processes.[4]

Adsorption-based cooling is an energy-efficient renewable-energy technology that can be driven using low-grade industrial waste heat and/or solar heat.[5] Porous materials like silica gel, activated carbon, and zeolites have been intensively studied as sorbents in adsorption-driven chillers and heat pumps. Thanks to the tunability of their chemical and structural features, MOFs have been recently considered as promising sorbents for adsorption cooling applications.[6] By using an industrially common fluorocarbon refrigerant R134a (1,1,1,2-tetrafluoroethane) as a model molecule, we found that surface area and pore volume of MOF sorbents alone cannot provide a suitable means for selecting high-performance sorbents.[7] Typically, hierarchical MOFs incorporating both micro-and mesopores exhibited a two-step adsorption isotherm to deliver large R134a uptake differences between high and low partial pressures.[7d] This highlights that there is still a great opportunity to purposely engineer the structures and pore topologies of the sorbent materials to shape preferable adsorption isotherm to benefit the application.[6a] This encouraged us to further explore the behavior of fluorocarbon adsorption into porous materials with even wider tunable pore organization.

[*] Dr. J. Zheng[+]
Department of Chemical Engineering, Sichuan University
Chengdu 610065 (P. R. China)
Dr. M. Wahiduzzaman,[+] Prof. Dr. G. Maurin
ICGM, Univ. Montpellier, CNRS, ENSCM
Montpellier (France)
E-mail: guillaume.maurin1@umontpellier.fr
Dr. D. Barpaga,[+] Dr. B. P. McGrail, Dr. R. K. Motkuri
Energy and Environment Directorate
Pacific Northwest National Laboratory
Richland, WA 99352 (USA)
E-mail: Radhakishan.Motkuri@pnnl.gov
Dr. B. A. Trump
Center for Neutron Diffraction
National Institute of Standards and Technology
Gaithersburg, MD 20899 (USA)
Dr. J. Zheng,[+] Dr. O. Y. Gutiérrez, Dr. P. Thallapally
Physical and Computational Sciences Directorate
Pacific Northwest National Laboratory
Richland, WA 99352 (USA)
Prof. Dr. S. Ma
Department of Chemistry, University of North Texas
Denton, TX 76201 (USA)
[+] These authors contributed equally to this work.
Supporting information and the ORCID identification number(s) for the author(s) of this article can be found under: https://doi.org/10.1002/anie.202102337.

© 2021 Wiley-VCH GmbH

These are not the final page numbers!

The introduction of defect sites into the structured frameworks is an efficient way to generate extra voids/porosities and modulate gas adsorption isotherm.[8] For example, the presence of missing linker and/or inorganic node defects in MOFs such as UiO-66 offered the opportunity to create additional porosity and accessible adsorption sites, which significantly enhanced the gas adsorption capability.[9] However, most MOFs contain long-range order and well-defined crystalline structure, which may limit further manipulation of the pore structure.[10] In the case of two-dimensional (2D) POFs, such as COFs or COPs, due to incomplete polymerization reaction, structural disorders and defects have been observed.[11] Such defects/disorders result from the presence of twisted conformation of 2D stacked layers, small sizes of the crystal domains, or *in-plane* interconnection missing.[12] These observations inspired us to kinetically control the linking chemistry to form desired defective pores during the irreversible condensation reaction for COP formation.

Currently, little is known how the defect sites in porous COPs affect their adsorption behaviors and performances for related applications; and how these metal-free porous COPs possess high surface area, large pore volume, and broad pore size distribution in the range of micro-and mesopores. To the best of our knowledge, the use of COPs as fluorocarbon sorbent materials for cooling applications is experimentally unprecedented. From a more fundamental standpoint, the construction of plausible atomistic models of defect-containing COPs and the prediction of their sorption properties has never been attempted so far. Thus, in this work, we explore the sorption performance of porous COPs, namely COP-2 and COP-3, for fluorocarbon R134a via a combination of experimental and modeling approaches.

The target porous COPs were synthesized via the self-polymerization of monomers tris(4-bromophenyl)amine and 1,3,5-tris(4-bromophenyl)benzene using nickel-catalyzed Yamamoto-type Ullmann cross-coupling reactions.[13] The two porous COPs were made of monomers containing either nitrogen atoms (COP-2) or benzene molecules (COP-3) respectively as connections (Figures 1a and S1 in supporting information). Inductively coupled plasma mass spectrometry (ICP-MS) measurements confirmed that the concentration of Ni used as a catalyst in the synthesis, is below the detection limit for both COPs. Powder and synchrotron *x*-ray diffraction (PXRD and SXRD) patterns (Figures S2 and S3), as well as TEM imaging (Figure S4), further revealed poor-long range crystallographic order for these two systems. Their N_2 sorption isotherms are characteristic of IUPAC type-II classification associated with a large type-IV hysteresis loop. Such a large hysteresis loop is attributed to the capillary condensation of N_2 in the mesoporosity of COPs that show a broad pore size distribution.[14] (Figure S5,S6). Figure 1b shows the experimentally derived pore size distribution (PSD) confirming the presence of not only expected micropores (<2 nm) but also mesopores (pores between 2–50 nm) of a broad size range. Furthermore, the measured pore volumes for COP-2 and COP-3 were determined to be 1.64 and 1.76 $cm^3 g^{-1}$, respectively (see Table S1). IR spectra confirm the formed functional groups in the two porous COPs (Figure S7).

Given the difficulty in the experimental structure determination of porous COPs owing to their poor-long range crystallographic order, previous attempts to propose structure models mostly relied on textural properties and microscopy imaging.[15] Therefore in earlier works, COP-2 and COP-3 have been described simply as graphene-analogues where little was known about the stacking arrangements and long-

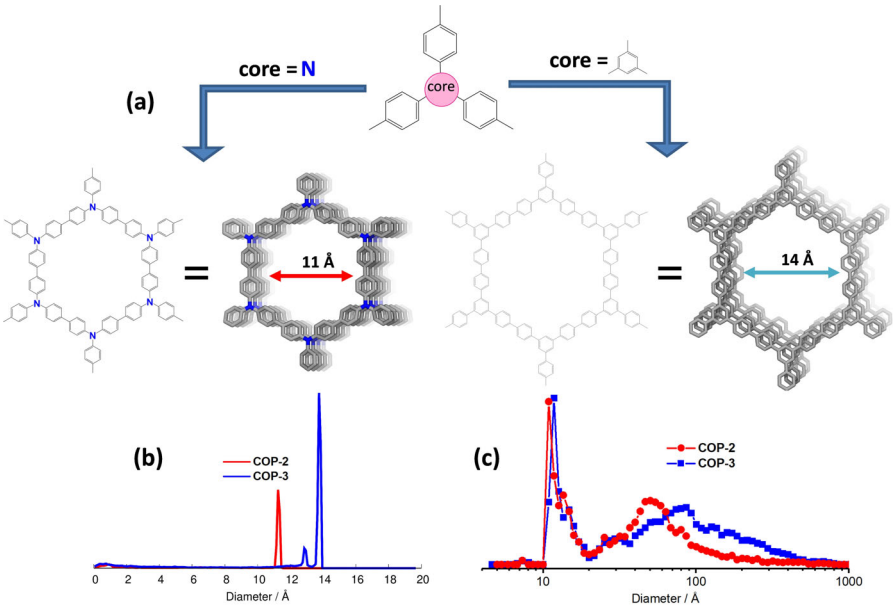

Figure 1. a) Schematics of porous COP-2 and COP-3 formation: The COPs with different cores were synthesized by using nickel-catalyzed Yamamoto-type Ullmann cross-coupling reactions at 105 °C. b) Pore size distributions of the energetically most stable DFT-derived defect-free COP-2 and COP-3 models. c) Pore size distributions of the experimentally synthesized COP-2 and COP-3 derived from N_2-sorption.

© 2021 Wiley-VCH GmbH

range ordering within these materials.[13,15,16] Later on, among others, Lukose et al. and Ongari et al. focused on the 2D layer arrangement of such systems employing quantum calculations.[17] In this context, herein we built various structure models of ordered, defect-free COP-2 and COP-3 by Density Functional Theory (DFT) calculations. The initial structure model of COP-3 was taken from the CURATED (Clean, Uniform, and Refined with Automatic Tracking from Experimental Database)[15] (Database of COFs ID: 10020N2). For the sake of a sound comprehension of the spatial conformation as well as the stacking arrangement, three different configurations were constructed and their geometries were fully optimized at the DFT level where both atomic positions and cell parameters were relaxed (see SI for details). These models comprise of two eclipsed AA stacking formed by either superimposed planar or non-planar layers (i.e., a relative twist of adjacent benzene rings) and one serrated inclined (non-planar) configuration, i.e., a marginal shift of odd layers associated with a constant offset in adjacent layers (see Figure S13).

In line with the conclusion drawn by Ongari et al.,[17a] both DFT optimized planar and non-planar eclipsed configurations for COP-3 remain trapped in the local minima maintaining the high symmetry (*P*6/*mmm* or *P*622) settings of the starting geometries. On the other hand, DFT optimization of the inclined-serrated configuration led to a much lower total energy leveraging the *P*1 symmetry setting, optimizing the conformation of the ligands as well as the shift in the layers to a favorable configuration that maximizes the non-covalent interactions. The significant drop of the DFT total energy for the inclined-serrated configuration (see Figure S13e) is accompanied by a reduction of its unit cell volume as well as its free pore volume as compared to those for the eclipsed counterparts (see Table S2). It is important to note that, since our DFT-optimization was carried out with a tight convergence criterion applied for atomic displacements and force gradients, the resulting inclined-serrated configuration shows slightly different interlayer offset and cell parameters compared to those previously reported by Ongari et al.[17a] Indeed, these calculations clearly demonstrated that the inclined-serrated configuration corresponds to the most energetically stable structure for COP-3 (see Figure S13e). Analysis of the pore size distribution (PSD) of these models revealed that both eclipsed stacking configurations possess pores of $\approx$16 Å dimension slightly wider than the inclined-serrated derivative ($\approx$14 Å). Similar structure models for COP-2 were then built from the associated molecular definition of the system (see Figure S14). In contrast to COP-3, it was found that COP-2 converges to an eclipsed stacking configuration irrespective of the initial starting geometries. Since the core part of COP-2 consists of a single N atom, assumingly, the N-N lone pair electronic interactions hold the layers superimposed. As such, the non-planar eclipsed stacking was found to be the most energetically stable structure for COP-2, which is characterized by a pore diameter of $\approx$11.0 Å, smaller than that of COP-3 (Figure S14).

Notably, these simulated PSD plots do not show a broad peak above 2 nm as observed experimentally for the two samples (Figures 1b and c). This difference emphasizes the presence of mesopores naturally occurring during the synthesis that is not obviously captured in these defect-free structure models. We also note that the calculated pore volumes for these COP-2 and COP-3 structure models range only from 0.83 to 1.29 $cm^3 g^{-1}$, respectively, much lower than the experimentally observed ones (1.64 to 1.76 $cm^3 g^{-1}$, see Table S1). This additional pore volume and observed larger pore size for the synthesized samples can be leveraged for harboring more accessible volume for the adsorbates yielding greater gas sorption equilibrium capacities.

To this end, R134a adsorption isotherms collected at 298 K and 308 K for COP-2 and COP-3 were reported in Figure 2, respectively. Interestingly, there is an initial sudden gas loading step at low pressure ($P < 50$ kPa). As the vapor pressure increases, the loading of R134a increases linearly above $P = 100$ kPa with a maximum uptake capacity of $\approx$180 wt% near-saturated pressure for both porous COPs. Uniquely, no plateau is observed for both isotherms even near the saturated pressure. A similar linearly increasing isotherm profile at higher pressures has been observed on 2D-COP (PAF-5) for alcohol adsorption by others, who evoked the possible presence of interconnection missing in the structure although not proved.[11a] Therefore, this R134a adsorption behavior is most probably attributed to the presence of large pores/defect sites present in the synthesized materials, which would lead to the adsorption of R134a first in the micropores and then to a gradual pore filling in large pores at higher pressure. The large spreading of adsorption-desorption hysteresis ($P < 100$ kPa to saturation pressure), indicates a wide

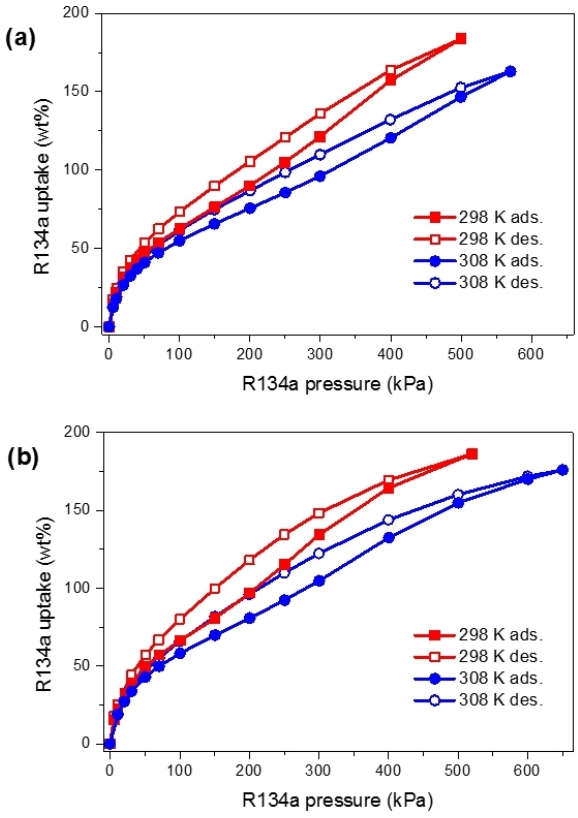

Figure 2. Adsorption isotherms of R134a in a) COP-2 and b) COP-3 measured at 298 K and 308 K.

© 2021 Wiley-VCH GmbH

These are not the final page numbers!

pore distribution of these COPs.[18] Furthermore, the similarity of the adsorption isotherms for COP-2 and COP-3 indicates that the different monomer connections, either nitrogen or benzene, have a minor influence on the adsorption behavior of R134a. It is also worth noting that the total R134a uptake in the two porous COPs ($\approx$ 180 wt %), is nearly fourfold higher than in the microporous Ni-MOF-74 and better than the mesoporous NU-1000 ($\approx$ 170 wt %) and most of the reported porous sorbents (Figure S8 and Table S8).[7d]

To gain deeper insight, the adsorption of R134a in COP-2 and COP-3 was further explored by means of force-field-based grand canonical Monte Carlo (GCMC) simulations (see SI for details, Figures S15, S16 and Tables S3–S6). The R134a adsorption isotherms were first calculated for the pristine defect-free COP models described above. Each of the pristine COP-2 and COP-3 models led to simulated adsorption type-I isotherms characteristic of microporous adsorbents (see Figure S22). Radial distribution functions (RDF) calculated for diverse R134a/COPs atom pairs at low coverage revealed that the defect-free COP-2 and COP-3 in their eclipsed AA planar configurations possess no particular anchoring sites for R134a since the separating R134a/COPs distances between F(R134a) and C(COP) are above 3 Å (see Figures S17 and S19). When AA eclipsed non-planar geometry is considered, the rotation of the phenyl rings makes possible an enhancement of the COPs/R134a interactions as seen by the shift at a lower distance of the corresponding RDF peaks (see Figures S18 and S20). This holds even more true for the COP-3 inclined-serrated model (see Figure S21). As such, the simulated R134a adsorption isotherm for the inclined-serrated COP-3 model shows a steeper rise at the low-pressure range compared to those calculated for the other eclipsed configurations (see Figure S22b). The same trend is observed when one compares the calculated adsorption isotherms for the AA eclipsed non-planar and planar COP-2 configurations (see Figure S22a). Figures 3 and S23 show that the simulated adsorption isotherms based on these defect-free models are at best able to reproduce the corresponding experimental data below $P/P_0 = 0.05$, i.e., the initial rise of the R134a adsorption in the micropore channels. Above this pressure range, the slope and shape of the simulated isotherms for these defect-free systems significantly deviate from the experimental ones. Notably, the experimental adsorption isotherms even surpassed the calculated maximum R134a uptakes at saturation in the defect-free COP-2 and COP-3 systems at $P/P_0 = 0.2$ and 0.3, respectively. This observation is consistent with the fact that the theoretical free volumes associated with these defect-free models drastically underestimate the pore volumes of the two synthesized samples (Table S2).

We further explored the R134a adsorption in COP defect-containing structure models. Since the eclipsed non-planar AA and inclined-serrated structures were found to be the most energetically stable ones for COP-2 and COP-3, respectively, a series of defect-containing models for these configurations corresponding to in-plane connection missing was constructed by sequentially removing core part and/or ligands to create incremental porosity and thus to gradually increase the free pore volume of the respective models. The

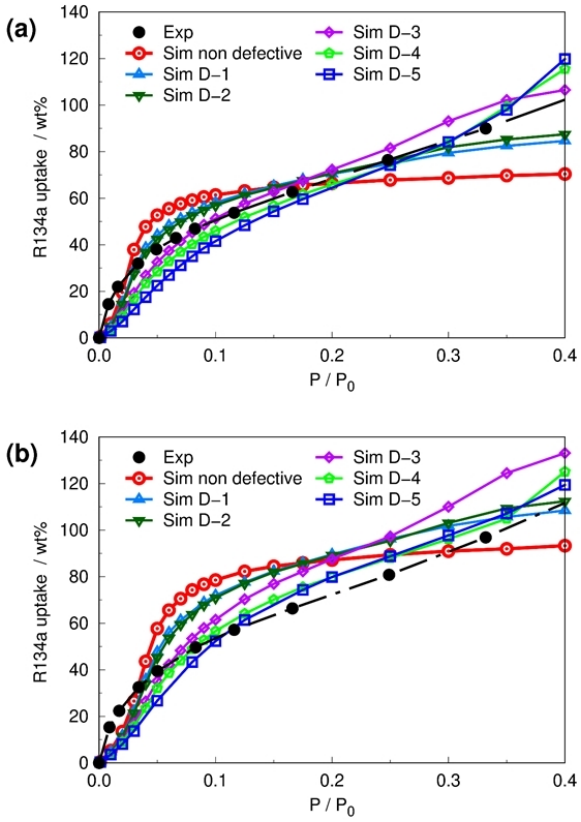

Figure 3. Comparison of experimental (black) and GCMC-simulated (colored) R134a adsorption isotherms at 298 K ($P_0 = 665$ kPa) in the pressure range 0–0.4 P/P_0 for the pristine and defect-containing COP-2 (a) and COP-3 (b) systems with a variable content of defects. COP-2 defect-free, D-1, D-2, D-3, D-4, and D-5 configurations correspond to free pore volumes of 0.87, 1.06, 1.27, 1.50, 1.63, and 1.70 $cm^3 g^{-1}$, respectively, while COP-3 pristine, D-1, D-2, D-3, D-4, and D-5 configurations correspond to free pore volumes of 1.01, 1.17, 1.22, 1.44, 1.73, and 1.90 $cm^3 g^{-1}$, respectively.

so-created COP-2 and COP-3 defect-containing structure models are presented in Table S7. These defect-containing models are denoted as D-1, D-2, D-3, D-4, and D-5 and associated with free pore volumes ranging from 1.03 to 1.70 $cm^3 g^{-1}$ and from 1.17 to 1.90 $cm^3 g^{-1}$, for COP-2 and COP-3, respectively. It is to be stressed that the size of these defect-containing models appears to be prohibitively expensive to fully relax them prior to adsorption simulations. As such, a representative defect-containing model D-4 of COP-3 with pore volumes 1.73 $cm^3 g^{-1}$—which represents nearly equal porosity of the corresponding synthesized system—was further geometry optimized at the density-functional tight-binding (DFTB) level. Notably, this DFTB optimized geometry remains close to the non-geometry optimized structure model (see ESI for details and Figure S24) leading to similar R134-a adsorption isotherms (Figure S25). Therefore, all the adsorption isotherms for the defect-containing COPs were calculated using the non-geometry optimized structure models.

The simulated adsorption isotherms reported in Figure 3 and S26 for all defect-containing structure models demonstrate that the creation of additional porosity allows not only to achieve higher adsorption uptake but also to capture the

 © 2021 Wiley-VCH GmbH

shape of the experimental adsorption isotherms in the intermediate pressure range more accurately. Typically, Figure S26 clearly shows that the consideration of COP-2 D-5 and COP-3 D-4 models with nearly equal porosities of the respective synthesized systems allows experimental equivalent maximum uptake of R-134a at high $P/P_0 = 0.85$. On the other hand, starting from defect-containing structure models D-3 to D-5 we can see an overall good reproduction of both shapes of the experimental isotherms and amount adsorbed for the two porous COPs up to $P/P_0 \approx 0.35$ to 0.4 (Figure 3). Figure 4 illustrates the distinct simulated pore filing of R134a in a series of defect-containing COP-3 for a given $P/P_0 = 0.2$. These snapshots clearly emphasize that the gradual increase of defects allows extra space that accommodates a higher loading of guest molecules. Figure S27 illustrates the sequential pore filling mechanism for COP-3 D4 configuration, which shows that the adsorption of R134a molecules starts in the more confined micropore channels followed by the adsorption in the mesopores.

Since the shapes of the isotherms in the low-pressure domain are better captured using these defect-containing structure models as compared with the pristine defect-free ones, this clearly implies that the synthesized porous COPs contain defects. However, above these pressure points, none of the defect-containing models are able to reproduce the linear shape of the experimental adsorption isotherm (Figure S26). This implies that a drastic change of the long-range ordering of both COPs is most probably guest-induced at higher pressure. Thus, even if conformation changes of the 2D stacked layers can be suspected, the guest-triggered defect dynamics cannot be emulated by the static simulations employed in this study considering any of our rigid defect-containing structure models.

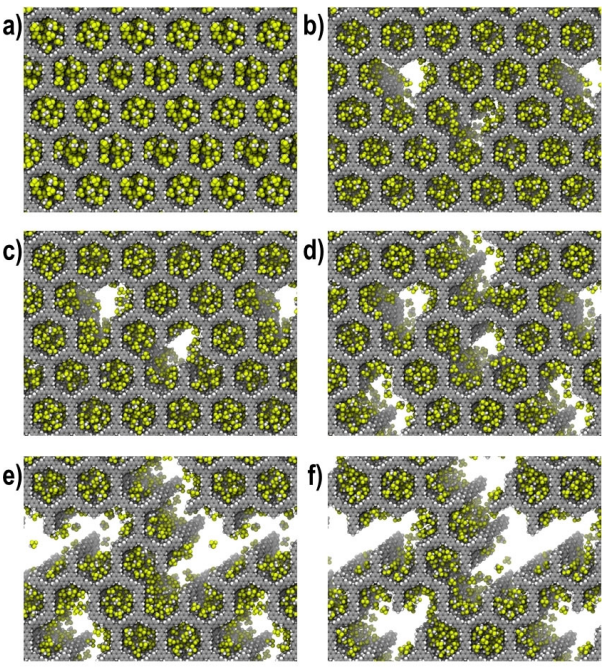

Figure 4. Illustration of the GCMC-derived snapshots of the adsorbed R134a molecules within the 1D channels of inclined-serrated COP-3 models at $P/P_0 = 0.20$ and 298 K: a) pristine defect-free model b) D-1, c) D-2, d) D-3, e) D-4, and f) D-5 defect-containing models associated with free pore volumes of 1.01, 1.17, 1.22, 1.44, 1.73, and 1.90 $cm^3 g^{-1}$, respectively.

Having attributed the unusual shape of the adsorption isotherms to the presence of defects in both porous COPs, it was worth exploring if this type of isotherm can be appealing for adsorption cooling. Since the sorption-based refrigeration cycle relies on a reversible adsorption/desorption process, the throughput of refrigerant (in this case, R134a) directly correlates to higher cooling potential. This throughput can be referred to as the difference in uptake between the adsorption and desorption steps, for which a more detailed explanation was provided previously elsewhere.[7b,d] Briefly, if this cycle is estimated to be only a pressure swing (isothermal working capacity), then the shape of the isotherm between these two pressures has a significant impact on the difference in uptakes between these two pressure points.[19] IUPAC type-I isotherm in comparison with linear-shaped isotherms will have varying sized windows of gas uptake as represented in the schematic provided in Figures S30a and S30b. Δm_a and Δm_b represent the isothermal working capacity calculated in the relative pressure ranges of $P/P_0 = 0.05$ to 0.3 (window a) and $P/P_0 = 0.2$ to 0.8 (window b). This Type-I isotherm shows a higher working capacity in the low-pressure region, which is beneficial to cryogenic applications. In contrast, a linear-shape isotherm (Figure S30b) with a high slope at moderate pressure range (not too low requiring a vacuum nor near saturation) has a more substantial potential for applicability in refrigeration processes.[20]

To quantify this impact, we have compared the difference in R134a uptake (Δm) between high ($P/P_0 = 0.8$) and low pressure ($P/P_0 = 0.2$) for the two investigated COPs as well as for several benchmark MOFs. These isothermal working capacities were calculated based on the experimentally collected adsorption isotherms (see the adsorption isotherms in Figure S8). COP-2 and COP-3 deliver working capacities of 116 wt.% and 114 wt.%, which are significantly higher than the performances of the MOF competitor NU-1000 ($\approx$75 wt.%) (Figure 5a). Higher working capacities directly impact the cooling capacities that emphasize the importance of having a unique linear-shaped isotherm observed in these COPs. As mentioned above, the absence of metallic elements in the porous COPs is expected to improve the reversibility and kinetics of gas adsorption-desorption cycles due to the weaker host-guest interactions. This is supported by the cyclic capacity in a closed system which remains constant even after 20 cycles. This reveals excellent sorption reversibility of R134a (Figures 5b, S6, and S12). We also interpreted the kinetic profile during R134a adsorption in the COPs (shown for COP-2 in Figure 5c and COP-3 in Figure S11). These profiles indicating a relatively short time (3–4 minutes) for R134a to equilibrate at a targeted pressure.

Further to provide direct evidence of weak host-guest interactions between the fluorocarbon and the COPs, calorimetry experiments have been employed (Figures 5d, S9, S10). The resulting differential adsorption enthalpies of R134a are much lower than the ΔH_{ads} values previously reported for MOFs. Both COP-2 and COP-3 have similar profiles showing an initial adsorption enthalpy of

© 2021 Wiley-VCH GmbH

These are not the final page numbers!

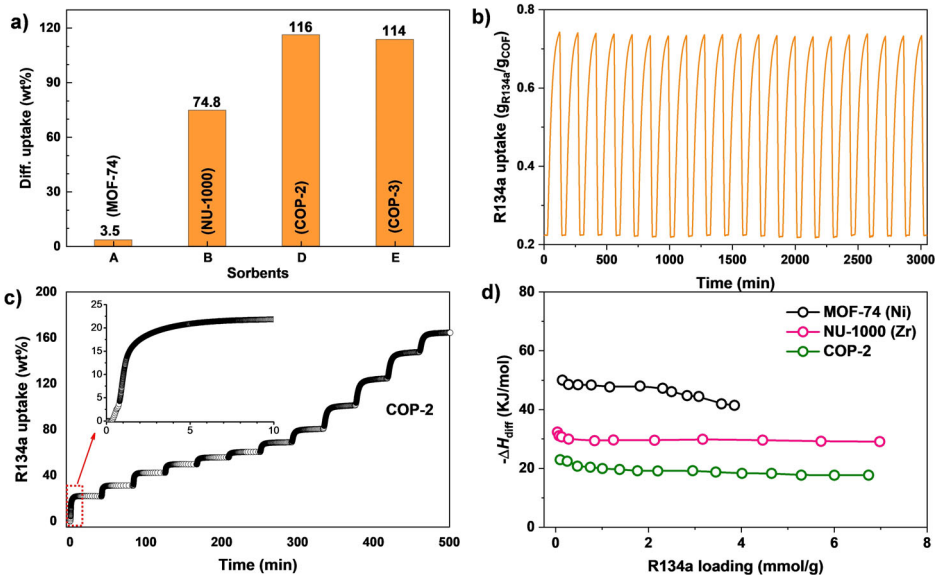

Figure 5. a) R134a working capacity of COPs compared with the state-of-the-art MOFs. b) 20 cycles of R134a adsorption/desorption in COP-2 via heating to 373 K and cooling to 298 K at a constant partial pressure of R134a (≈1.5 bar). c) Kinetic profile during R134a adsorption in COP-2 for 500 min. The plateaus represent target pressures at each adsorption isotherm point for which the instrument measures gas uptake. Inset: Zoomed-in view of the first 10 min. d) Comparison of differential adsorption enthalpies during R134a adsorption for COPs investigated here and state-of-the-art MOFs.

≈24 kJ mol^{-1}, far lower than the values reported for Zr-NU-1000 (≈32 kJ mol^{-1})[7d] and Ni-MOF-74 (≈50 kJ mol^{-1})[7c] which are associated with relatively strong interactions between R134a and the MOF adsorption sites. These experimental findings are consistent with the conclusions drawn from our GCMC simulations for the defect-containing COP-2 and COP-3 structure models that revealed adsorption enthalpy of about 25 kJ mol^{-1} resulting from moderate interactions between F atoms of R134a and C atoms of the COPs (see Figures S28 and S29) in a similar way that observed above for the defect-free COP-2 and COP-3. Furthermore, due to the presence of more confined pores, the calculated adsorption enthalpy for defect-free COPs are slightly higher (≈30 kJ mol^{-1}) than their defect-containing counterparts. Ultimately the combination of kinetics and calorimetry data indicate that fast sorption behavior might be benefited from both relatively weak sorbate-sorbent interactions and large pores which leads to high R134a diffusion rates across the material. These relatively weak host-guest interactions are more favorable for applicability in a refrigeration cycle where minimizing energy requirements for desorption is necessary to overcome adsorption enthalpies.

Conclusion

In conclusion, to the best of our knowledge, we report for the first time, the adsorption behavior of R134a on porous COP materials, specifically COP-2 and COP-3, which both show unique linear-shaped isotherms leading to uptake at 600 kPa exceeding that of most of the porous materials reported so far. The GCMC simulated adsorption isotherms for defect-containing structure models integrating micro- and mesopores created by missing-in-plane connections and with pore volumes matching the experimental ones captured the saturation uptake and the shape of the experimental isotherms up to an intermediate pressure range ($P/P_0 = 0.40$). However, these calculations failed to reproduce the linear regime at a higher pressure that suggests a substantial guest-induced pore reorganization, for example, conformation changes of 2D stacked layers, in this pressure range. The unique isotherm shape displayed by these two porous COPs combined with fast kinetics of adsorption and very high working capacities were further found to be appealing for reversible cycles of sorption in sorbent-based cooling applications. The fundamental knowledge gained on the structure of defect-containing porous covalent organic polymers and their unique adsorption behavior paves the way towards their exploitation in a myriad of adsorption-driven applications.

Acknowledgements

The authors acknowledge the U.S. Military Sealift Command and the U.S. Department of Energy (DOE), Energy Efficiency and Renewable Energy's Geothermal Technologies Office (GTO) for financial support. O.Y.G. and R.K.M. also acknowledge the Inorganometallic Catalyst Design Center, an EFRC funded by the U.S. Department of Energy (DOE), Office of Science, Office of Basic Energy Sciences (DE-SC0012702). PNNL is operated by Battelle for the U.S. Department of Energy (DOE) under Contract DE-AC05-76RL01830. This work was granted access to the HPC resources of CINES under the allocation A0100907613 made by GENCI.

 © 2021 Wiley-VCH GmbH

Conflict of interest

The authors declare no conflict of interest.

Keywords: adsorption cooling · structure defects · fluorocarbon refrigerants · porous covalent organic polymers

[1] a) P. J. Waller, F. Gandara, O. M. Yaghi, *Acc. Chem. Res.* **2015**, *48*, 3053 – 3063; b) A. P. Cote, A. I. Benin, N. W. Ockwig, M. O'Keeffe, A. J. Matzger, O. M. Yaghi, *Science* **2005**, *310*, 1166 – 1170; c) Z. H. Xiang, D. P. Cao, L. M. Dai, *Polym. Chem.* **2015**, *6*, 1896 – 1911; d) X. Zhu, Y. Y. Hua, C. C. Tian, C. W. Abney, P. Zhang, T. Jin, G. P. Liu, K. L. Browning, R. L. Sacci, G. M. Veith, H. C. Zhou, W. Q. Jin, S. Dai, *Angew. Chem. Int. Ed.* **2018**, *57*, 2816 – 2821; *Angew. Chem.* **2018**, *130*, 2866 – 2871; e) S. H. Zhang, Q. Yang, C. Wang, X. L. Luo, J. H. Kim, Z. Wang, Y. Yamauchi, *Adv. Sci.* **2018**, *5*, 1801116; f) T. Hasell, A. I. Cooper, *Nat. Rev. Mater.* **2016**, *1*, 16053.

[2] a) N. Huang, P. Wang, D. L. Jiang, *Nat. Rev. Mater.* **2016**, *1*, 16068; b) P. Puthiaraj, Y. R. Lee, S. Q. Zhang, W. S. Ahn, *J. Mater. Chem. A* **2016**, *4*, 16288 – 16311; c) S. Che, J. Pang, A. J. Kalin, C. Wang, X. Ji, J. Lee, D. Cole, J.-L. Li, X. Tu, Q. Zhang, H.-C. Zhou, L. Fang, *ACS Mater. Lett.* **2020**, *2*, 49 – 54; d) M. J. Strauss, A. M. Evans, I. Castano, R. L. Li, W. R. Dichtel, *Chem. Sci.* **2020**, *11*, 1957 – 1963; e) S. Y. Ding, M. Dong, Y. W. Wang, Y. T. Chen, H. Z. Wang, C. Y. Su, W. Wang, *J. Am. Chem. Soc.* **2016**, *138*, 3031 – 3037; f) Y. S. Lan, X. H. Han, M. M. Tong, H. L. Huang, Q. Y. Yang, D. H. Liu, X. Zhao, C. L. Zhong, *Nat. Commun.* **2018**, *9*, 5274.

[3] a) S. Y. Ding, W. Wang, *Chem. Soc. Rev.* **2013**, *42*, 548 – 568; b) Z. H. Xiang, R. Mercado, J. M. Huck, H. Wang, Z. H. Guo, W. C. Wang, D. P. Cao, M. Haranczyk, B. Smit, *J. Am. Chem. Soc.* **2015**, *137*, 13301 – 13307; c) H. A. Patel, S. H. Je, J. Park, D. P. Chen, Y. Jung, C. T. Yavuz, A. Coskun, *Nat. Commun.* **2013**, *4*, 1357; d) R. Babarao, J. W. Jiang, *Energy Environ. Sci.* **2008**, *1*, 139 – 143.

[4] H. Wang, Z. Zeng, P. Xu, L. Li, G. Zeng, R. Xiao, Z. Tang, D. Huang, L. Tang, C. Lai, D. Jiang, Y. Liu, H. Yi, L. Qin, S. Ye, X. Ren, W. Tang, *Chem. Soc. Rev.* **2019**, *48*, 488 – 516.

[5] a) IEA (Ed.: I. E. Agency), International Energy Agency, **2018**; b) M. F. de Lange, K. J. F. M. Verouden, T. J. H. Vlugt, J. Gascon, F. Kapteijn, *Chem. Rev.* **2015**, *115*, 12205 – 12250.

[6] a) S. Wang, J. S. Lee, M. Wahiduzzaman, J. Park, M. Muschi, C. Martineau-Corcos, A. Tissot, K. H. Cho, J. Marrot, W. Shepard, G. Maurin, J. S. Chang, C. Serre, *Nat. Energy* **2018**, *3*, 985 – 993; b) J. Liu, J. Zheng, D. Barpaga, S. Sabale, B. Arey, M. A. Derewinski, B. P. McGrail, R. K. Motkuri, *Eur. J. Inorg. Chem.* **2018**, 885 – 889; c) Z. W. Mo, H. L. Zhou, D. D. Zhou, R. B. Lin, P. Q. Liao, C. T. He, W. X. Zhang, X. M. Chen, J. P. Zhang, *Adv. Mater.* **2018**, *30*, 1704350; d) H. Wang, L. Yu, Y. Lin, J. Peng, S. J. Teat, L. J. Williams, J. Li, *Inorg. Chem.* **2020**, *59*, 4167 – 4171; e) H. Y. Chen, Z. J. Chen, O. K. Farha, R. Q. Snurr, *ACS Sustainable Chem. Eng.* **2019**, *7*, 18242 – 18246; f) H. Y. Chen, Z. J. Chen, L. Zhang, P. Li, J. Liu, L. R. Redfern, S. Moribe, Q. Cui, R. Q. Snurr, O. K. Farha, *Chem. Mater.* **2019**, *31*, 2702 – 2706; g) D. Barpaga, M. Shetty, J. Zheng, H. Wang, B. P. McGrail, R. K. Motkuri, *Inorg. Chem.* **2020**, *59*, 15620 – 15625.

[7] a) R. K. Motkuri, H. V. R. Annapureddy, M. Vijaykumar, H. T. Schaef, P. F. Martin, B. P. McGrail, L. X. Dang, R. Krishna, P. K. Thallapally, *Nat. Commun.* **2014**, *5*, 4368; b) J. Zheng, D. Barpaga, B. Trump, M. Shetty, Y. Fan, P. Bhattacharya, J. Jenks, C.-Y. Su, C. M. Brown, G. Maurin, B. P. McGrail, R. K. Motkuri, *J. Am. Chem. Soc.* **2020**, *142*, 3002 – 3012; c) J. Zheng, R. S. Vemuri, L. Estevez, P. K. Koech, T. Vargas, D. M. Camaioni, T. A. Blake, B. P. McGrail, R. K. Motkuri, *J. Am. Chem. Soc.* **2017**, *139*, 10601 – 10604; d) J. Zheng, D. Barpaga, O. Y. Gutiérrez, N. D. Browning, B. L. Mehdi, O. K. Farha, J. A. Lercher, B. P. McGrail, R. K. Motkuri, *ACS Appl. Energy Mater.* **2018**, *1*, 5853 – 5858.

[8] a) S. H. Yang, X. Lin, W. Lewis, M. Suyetin, E. Bichoutskaia, J. E. Parker, C. C. Tang, D. R. Allan, P. J. Rizkallah, P. Hubberstey, N. R. Champness, K. M. Thomas, A. J. Blake, M. Schroder, *Nat. Mater.* **2012**, *11*, 710 – 716; b) Z. L. Fang, B. Bueken, D. E. De Vos, R. A. Fischer, *Angew. Chem. Int. Ed.* **2015**, *54*, 7234 – 7254; *Angew. Chem.* **2015**, *127*, 7340 – 7362; c) C. Serre, *Nature* **2013**, *493*, 313 – 314; d) H. H. Mautschke, F. Drache, I. Senkovska, S. Kaskel, F. X. L. I. Xamena, *Catal. Sci. Technol.* **2018**, *8*, 3610 – 3616; e) M. Ishizaki, S. Akiba, A. Ohtani, Y. Hoshi, K. Ono, M. Matsuba, T. Togashi, K. Kananizuka, M. Sakamoto, A. Takahashi, T. Kawamoto, H. Tanaka, M. Watanabe, M. Arisaka, T. Nankawa, M. Kurihara, *Dalton Trans.* **2013**, *42*, 16049 – 16055.

[9] a) P. Ghosh, Y. J. Colon, R. Q. Snurr, *Chem. Commun.* **2014**, *50*, 11329 – 11331; b) O. Kozachuk, I. Luz, F. X. L. I. Xamena, H. Noei, M. Kauer, H. B. Albada, E. D. Bloch, B. Marler, Y. M. Wang, M. Muhler, R. A. Fischer, *Angew. Chem. Int. Ed.* **2014**, *53*, 7058 – 7062; *Angew. Chem.* **2014**, *126*, 7178 – 7182; c) S. Waitschat, D. Frohlich, H. Reinsch, H. Terraschke, K. A. Lomachenko, C. Lamberti, H. Kummer, T. Helling, M. Baumgartner, S. Henningerb, N. Stock, *Dalton Trans.* **2018**, *47*, 1062 – 1070.

[10] a) D. Barpaga, J. Zheng, K. S. Han, J. A. Soltis, V. Shutthanandan, S. Basuray, B. P. McGrail, S. Chatterjee, R. K. Motkuri, *Inorg. Chem.* **2019**, *58*, 8339 – 8346; b) J. Zheng, J. Y. Ye, M. A. Ortuno, J. L. Fulton, O. Y. Gutierrez, D. M. Camaioni, R. K. Motkuri, Z. Y. Li, T. E. Webber, B. L. Mehdi, N. D. Browning, R. L. Penn, O. K. Farha, J. T. Hupp, D. G. Truhlar, C. J. Cramer, J. A. Lercher, *J. Am. Chem. Soc.* **2019**, *141*, 9292 – 9304; c) M. H. Mohamed, Y. H. Yang, L. Li, S. Zhang, J. P. Ruffley, A. G. Jarvi, S. Saxena, G. Veser, J. K. Johnson, N. L. Rosi, *J. Am. Chem. Soc.* **2019**, *141*, 13003 – 13007; d) L. Y. Li, L. D. Guo, Z. G. Zhang, Q. W. Yang, Y. W. Yang, Z. Bao, Q. L. Ren, J. Li, *J. Am. Chem. Soc.* **2019**, *141*, 9358 – 9364.

[11] a) H. Ren, T. Ben, F. X. Sun, M. Y. Guo, X. F. Jing, H. P. Ma, K. Cai, S. L. Qiu, G. S. Zhu, *J. Mater. Chem.* **2011**, *21*, 10348 – 10353; b) Y. P. Song, Q. Sun, B. Aguila, S. Q. Ma, *Adv. Sci.* **2019**, *6*, 1801410.

[12] a) Z. H. Xiang, D. P. Cao, W. C. Wang, W. T. Yang, B. Y. Han, J. M. Lu, *J. Phys. Chem. C* **2012**, *116*, 5974 – 5980; b) V. Nguyen, M. Grunwald, *J. Am. Chem. Soc.* **2018**, *140*, 3306 – 3311; c) S. Kandambeth, K. Dey, R. Banerjee, *J. Am. Chem. Soc.* **2019**, *141*, 1807 – 1822.

[13] Z. H. Xiang, X. Zhou, C. H. Zhou, S. Zhong, X. He, C. P. Qin, D. P. Cao, *J. Mater. Chem.* **2012**, *22*, 22663 – 22669.

[14] W. D. Machin, R. J. Murdey, *Langmuir* **1996**, *12*, 6501 – 6505.

[15] a) T. Ben, K. Shi, Y. Cui, C. Y. Pei, Y. Zuo, H. Guo, D. L. Zhang, J. Xu, F. Deng, Z. Q. Tian, S. L. Qiu, *J. Mater. Chem.* **2011**, *21*, 18208 – 18214; b) S. Aparicio, C. T. Yavuz, M. Atilhan, *ChemistrySelect* **2018**, *3*, 8294 – 8305.

[16] a) Z. H. Xiang, Q. B. Dai, J. F. Chen, L. M. Dai, *Adv. Mater.* **2016**, *28*, 6253 – 6261; b) Z. H. Xiang, D. P. Cao, *Macromol. Rapid Commun.* **2012**, *33*, 1184 – 1190.

[17] a) D. Ongari, A. V. Yakutovich, L. Talirz, B. Smit, *ACS Cent. Sci.* **2019**, *5*, 1663 – 1675; b) B. Lukose, A. Kuc, T. Heine, *Chem. Eur. J.* **2011**, *17*, 2388 – 2392.

[18] Z. P. Bažant, M. Z. Bazant, *J. Mech. Phys. Solids* **2012**, *60*, 1644 – 1659.

[19] G. D. Pirngruber, L. Hamon, S. Bourrelly, P. L. Llewellyn, E. Lenoir, V. Guillerm, C. Serre, T. Devic, *ChemSusChem* **2012**, *5*, 762 – 776.

[20] J. J. Jenks, R. K. Motkuri, W. TeGrotenhuis, B. K. Paul, B. P. McGrail, *Heat Transfer Eng.* **2017**, *38*, 1305 – 1315.

Manuscript received: February 15, 2021
Accepted manuscript online: April 27, 2021
Version of record online: ■■ ■■, ■■■■

 © 2021 Wiley-VCH GmbH

These are not the final page numbers!

Research Articles

Porous Materials

J. Zheng, M. Wahiduzzaman, D. Barpaga, B. A. Trump, O. Y. Gutiérrez, P. Thallapally, S. Ma, B. P. McGrail, G. Maurin,* R. K. Motkuri* _____ ▮▮▮▮–▮▮▮▮

Porous Covalent Organic Polymers for Efficient Fluorocarbon-Based Adsorption Cooling

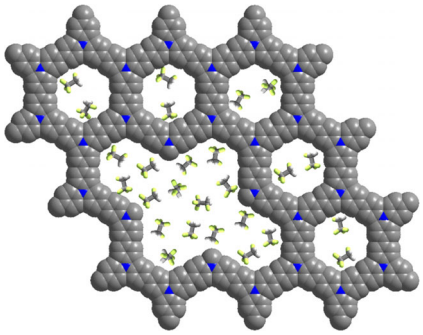

The first joint experimental–computational study of fluorocarbon adsorption into porous covalent organic polymers (COPs) reveals that the presence of structure defects leading to the creation of mesopores with a broad size range offers not only exceptional high-uptake adsorption of fluorocarbon R134a, but also unique overall linear-shaped isotherms. COPs are thus proven to be excellent sorbent materials for cooling applications.

© 2021 Wiley-VCH GmbH